APPLIED SCIENCES AND ENGINEERING

Multiple-wavelength neutron holography with pulsed neutrons

Kouichi Hayashi,[1]* Kenji Ohoyama,[2] Naohisa Happo,[3] Tomohiro Matsushita,[4] Shinya Hosokawa,[5] Masahide Harada,[6] Yasuhiro Inamura,[6] Hiroaki Nitani,[7] Toetsu Shishido,[8] Kunio Yubuta[8]

Local structures around impurities in solids provide important information for understanding the mechanisms of material functions, because most of them are controlled by dopants. For this purpose, the x-ray absorption fine structure method, which provides radial distribution functions around specific elements, is most widely used. However, a similar method using neutron techniques has not yet been developed. If one can establish a method of local structural analysis with neutrons, then a new frontier of materials science can be explored owing to the specific nature of neutron scattering—that is, its high sensitivity to light elements and magnetic moments. Multiple-wavelength neutron holography using the time-of-flight technique with pulsed neutrons has great potential to realize this. We demonstrated multiple-wavelength neutron holography using a Eu-doped CaF_2 single crystal and obtained a clear three-dimensional atomic image around trivalent Eu substituted for divalent Ca, revealing an interesting feature of the local structure that allows it to maintain charge neutrality. The new holography technique is expected to provide new information on local structures using the neutron technique.

INTRODUCTION

The history of atomic-resolution holography started in 1986 (*1*) with the concepts of photoelectron (*2*) and x-ray fluorescence holography, (*3*), which generated important applications to adsorbates (*4*), dopants (*5*, *6*), and disordered systems (*7*). A major advantage of atomic-resolution holography is the visualization of three-dimensional (3D) atomic images around a specific element in a region up to a few nanometers from the element without previous knowledge of the structure. Novel achievements using x-ray fluorescence holography have been reported, including the discovery of suboxide nanoclusters in a high–Curie temperature (Tc) ferromagnetic semiconductor (*6*) and the determination of the rhombohedral distortion of a crystal unit cell in a relaxor ferroelectric (*7*). These achievements were based on the use of a multiple-wavelength holography method, which is a highly efficient (*8*), but time-consuming, method for obtaining accurate atomic images. On the other hand, a single-energy hologram cannot provide a reliable 3D atomic image owing to the lack of information in the hologram.

In 2001, Sur *et al.* (*9*) first demonstrated the use of neutron holography to visualize the 3D local structure around hydrogen atoms, and Cser *et al.* (*10*) applied the method to dopants in 2002. Neutron holography can also potentially be used to visualize atoms of light elements and magnetic moments. However, all previous studies were carried out by a single-wavelength holography method (*11*–*14*). The main reason why the single-wavelength mode has been used is the weakness of a monochromatic neutron beam whose flux is typically six orders of magnitude smaller than that of an x-ray beam from a third-generation synchrotron radiation source.

To overcome this disadvantage, neutron researchers have developed the time-of-flight technique using pulsed neutrons from spallation neutron sources (*15*). Because this technique can select the wavelengths of neutrons from their times of flight, the monochromatization of neutron beams is not necessary, in contrast to x-ray techniques. Its advantage is that the entire wavelength range of white neutrons can be used for experiments without the loss of emitted neutrons from the source. Thus, the time-of-flight technique is very suitable for multiple-wavelength neutron holography, which we have demonstrated in the present study.

There are two modes in neutron holography: internal source and internal detector holography modes. Here, we adopted the internal detector mode (*10*). Figure 1A shows a schematic illustration of neutron holography combined with the time-of-flight technique. As a result of collisions of high-energy protons with a heavy element such as Hg, white neutrons are generated with a pulse-shaped time structure, meaning that all the neutrons with different wavelengths are ejected from the target. The neutron wavelength, λ, which is inversely proportional to the neutron velocity, is obtained from the time of flight from the spallation source to the sample using the equation $\lambda = 3956/\upsilon = 3956 \times (\mathrm{ToF}/L)$, where υ, L, and ToF are the neutron velocity (in meters per second), the distance (in meters) between the spallation source and the sample, and the time of flight (ToF) (in seconds), respectively. Because the Eu nuclei in the sample used in this study emit γ rays upon absorbing neutrons, a time-of-flight spectrum of the γ ray intensity is created (Fig. 1B). In the internal detector mode, a hologram represents the 2D angular dependence of the γ ray intensity on the sample orientation at each wavelength of the neutrons, as shown in Fig. 1C (*8*, *11*). In the sample, the direct (reference) and scattered (object) neutron waves form weak neutron standing waves. A target atom senses this standing-wave field, which varies with the direction and wavelength of the incoming neutrons, and then emits γ rays with a frequency proportional to its amplitude; the target atom acts as a wave field detector. In Fig. 1 (D and E), we show two examples of neutron holography at ToF = t_1 and t_3, namely, at short and long wavelengths, respectively. As shown in these figures, different standing-wave patterns are formed depending on the time of flight, and consequently, holograms with different wavelengths can be measured. Because the time of flight can be partitioned into ~40,000 segments

[1]Frontier Research Institute for Materials Research, Nagoya Institute of Technology, Nagoya 466-8555, Japan. [2]Graduate School of Science and Engineering, Ibaraki University, Hitachi 316-8511, Japan. [3]Graduate School of Information Sciences, Hiroshima City University, Hiroshima 731-3194, Japan. [4]Japan Synchrotron Radiation Research Institute, Sayo, Hyogo 679-5198, Japan. [5]Department of Physics, Kumamoto University, Kumamoto 860-8555, Japan. [6]Materials and Life Science Division, J-PARC Center, Japan Atomic Energy Agency, Tokai, Ibaraki 319-1195, Japan. [7]Institute of Materials Structure Science, High Energy Accelerator Research Organization (KEK), Tsukuba 305-0801, Japan. [8]Institute for Materials Research, Tohoku University, Sendai 980-8577, Japan.
*Corresponding author. Email: khayashi@nitech.ac.jp

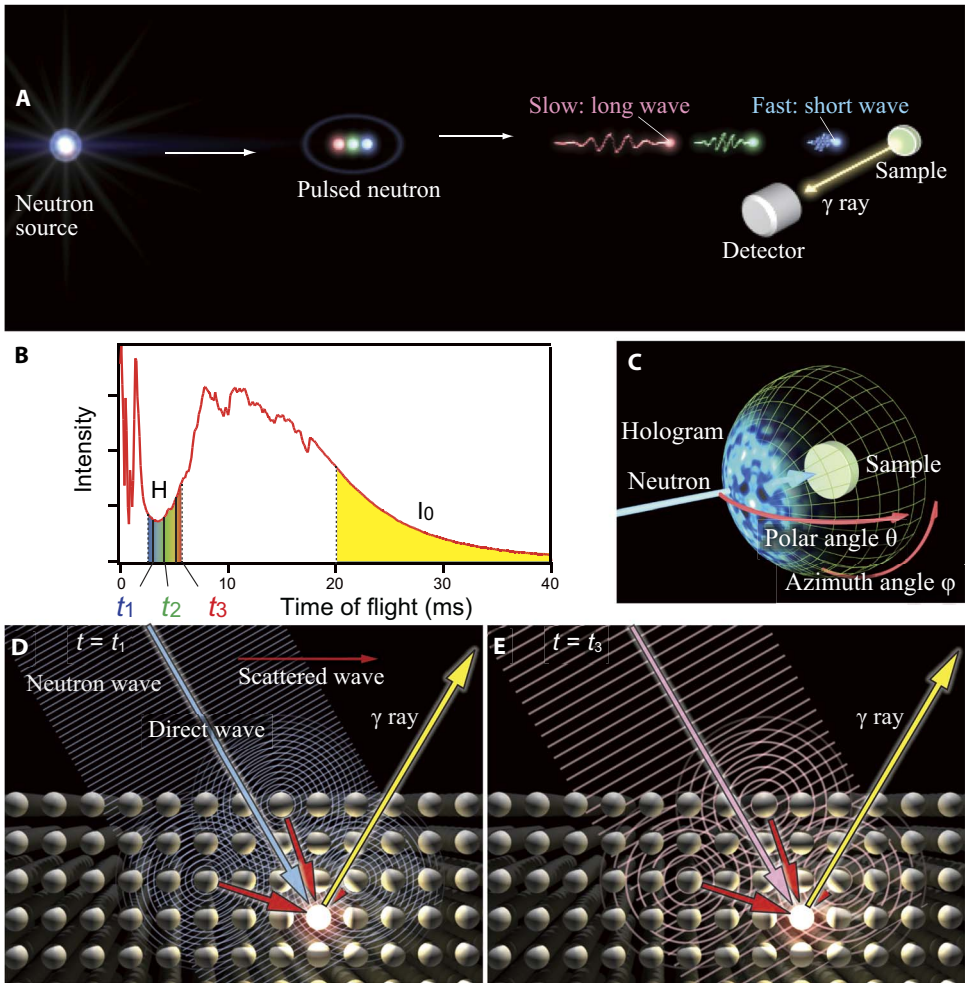

Fig. 1. Illustrations of the principle of multiple-wavelength neutron holography and the experimental setup. (**A**) Schematic drawing of the experimental setup. (**B**) Time-of-flight spectrum from Eu in CaF_2. (**C**) Concept of hologram recording. The hologram represents the γ ray intensity as a function of the azimuthal angle φ and polar angle θ. (**D** and **E**) Principle of neutron holography in the internal detector mode. The times of flight of the neutrons in (D) and (E) are ToF = t_1 and t_3, respectively.

by a signal processor, a number of holograms with different wavelengths can be collected by a single angular scan in principle (see Materials and Methods).

RESULTS

We carried out a neutron experiment at beamline BL10 (*16*) of the neutron spallation source facility of J-PARC (Japan Proton Accelerator Research Complex), Tokai, Japan (*17*). The measured sample was a 1 atomic % (at %) Eu-doped CaF_2 single crystal, which is often used for scintillators (*18*). The sample was mounted on a two-axis goniometer, and γ rays from the sample were detected by a scintillation counter. Figure 2A shows a photograph of the experimental setup. The neutron absorption cross section of a Eu nucleus is ~10^5 times larger than the cross sections of Ca and F nuclei, meaning that the γ ray intensity from Ca and F is negligible in the experiment (*19*). The wavelength in the time-of-flight spectrum in Fig. 1B ranges from 0.1 to 11.3 Å. In particular, between 0.77 and 1.57 Å (the rainbow-colored region), we divided the spectrum into 34 wavelength regions. This is greater than the number of wavelengths in multiple-wavelength x-ray fluorescence holograms (typically 8 to 10), and it significantly contributes to the generation of accurate atomic images with minimum ghosts. We processed the time-of-flight spectra in the entire range of angles ϕ (0° to 360°) and θ (20° to 160°). The amplitudes of the experimental holograms were decreased by the absorption effect of neutrons and γ rays. Therefore, we estimated the absorption effect using the geometric model in Fig. 2B and obtained the decrement in the holographic amplitude, as shown in Fig. 2C (*20*). After the correction for absorption and the symmetrization of the measured holograms using the crystal symmetry of CaF_2, we finally obtained the holograms displayed in Fig. 3. Figure 3A shows the multiple-wavelength hologram obtained by superimposing holograms for 34 different wavelengths along the radial direction. Because this volume hologram is displayed in k space, the wavelength is converted to $|\mathbf{k}|$ (=$2\pi/\lambda$) (Fig. 3A). Figure 3B shows the hologram at $|\mathbf{k}| = 4.05$ Å^{-1} ($\lambda = 1.55$ Å), extracted from the multiple-wavelength hologram. Note that lines corresponding to neutron standing waves are visible in Fig. 3B, indicating that we succeeded in observing the local symmetry around Eu.

From the volume hologram, we successfully reconstructed a real-space image around Eu using the Barton multiple-wavelength reconstruction

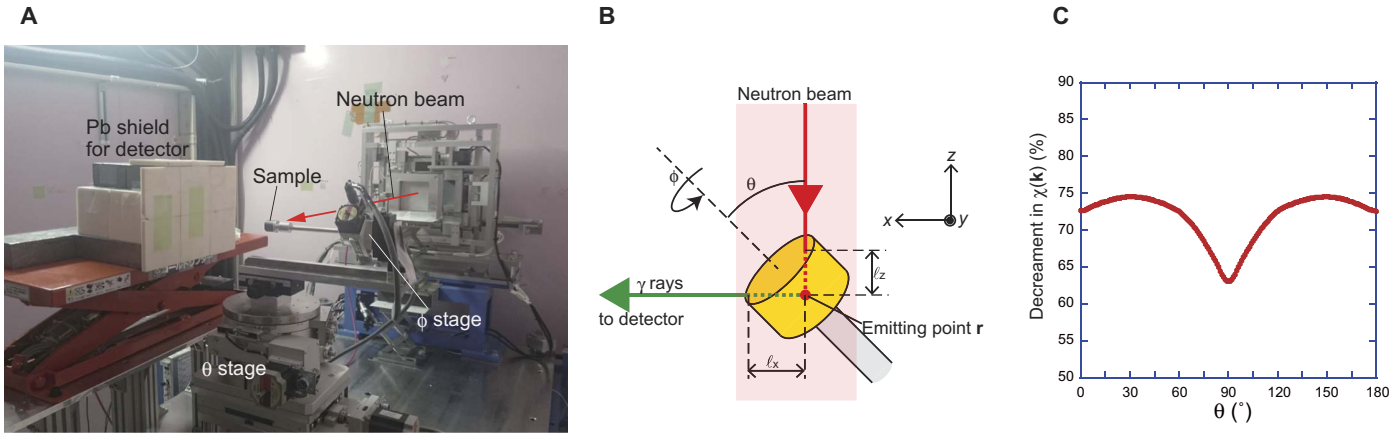

Fig. 2. Setup for multiple-wavelength neutron holography and absorption effect on holographic amplitude. (**A**) Photograph. (**B**) Schematic of geometry used for consideration of the absorption effect. (**C**) Decrement in the holographic amplitude due to the absorption effect.

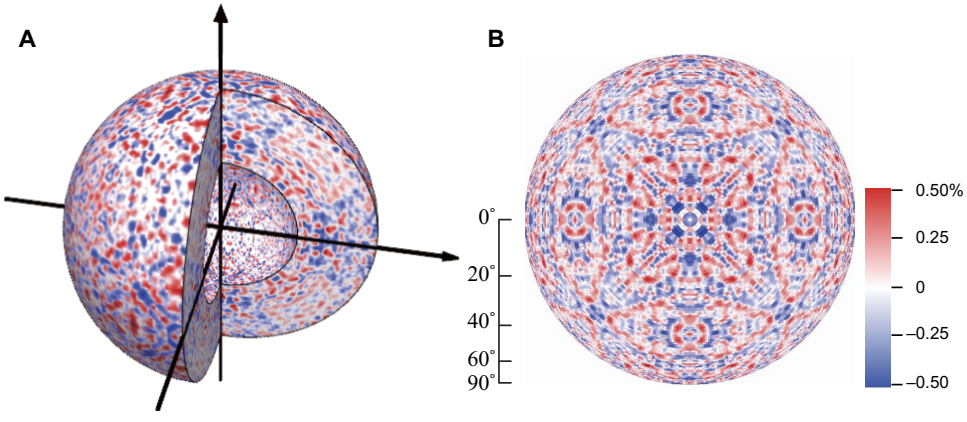

Fig. 3. Neutron holograms of environmental structure around Eu in CaF_2. (**A**) Volume hologram. (**B**) 2D hologram at $|\mathbf{k}| = 4.05$ Å^{-1}.

algorithm (*21*), as shown in Fig. 4. The images in Fig. 4 (A and B) are experimentally and theoretically reconstructed atomic images, respectively. The theoretical reconstruction was obtained from the calculated holograms using a model in which Eu atoms substitute for Ca atoms in CaF_2. Comparing the two real-space images, we found significant differences at the nearest Ca positions. These Ca atomic images are split into two parts. This indicates displacements of the Ca atoms from the ideal positions. To discuss the local structure more quantitatively, we obtained cross sections of the 3D experimental images at the Ca and F planes, as shown in Fig. 5.

To obtain further information on the local structure around Eu, we measured x-ray absorption fine structure (XAFS) spectra for our sample. Figure 6A shows the x-ray absorption near edge structure (XANES) spectra of the Eu-doped CaF_2 and a standard sample of Eu_2O_3 at room temperature. A strong peak was observed at $E = 6.981$ keV, which is in good agreement with that of Eu_2O_3, indicating that the doped Eu in CaF_2 is trivalent at the position of Ca^{2+}. On the other hand, a small shoulder was observed at approximately $E = 6.975$ keV, implying that a small amount of Eu^{2+} exists. Figure 6B shows the radial distribution function obtained by the Fourier transformation of the extended XAFS (EXAFS) oscillation. By analyzing the peak at 1.84 Å, we determined the bond length of Eu–F to be 2.37 Å, which is close to the position of F^- obtained from the neutron holography experiments. Moreover, the interatomic distance between Eu and Ca was also determined to be 4.00 Å from the peak at 3.5 Å, which is 0.13 Å longer than the Ca–Ca distance (3.87 Å) in pure CaF_2 crystal.

DISCUSSION

Some researchers have asserted that modification of a local structure is stabilized by the capture of an additional fluoride ion (F^-), which might be located at a neighbor interstitial position (*22*, *23*). The possible locations are indicated by the crosses in Fig. 5A. At the conventional contrast scale, no images can be seen around the crosses, which is reasonable because of the very low occupancy of F^- at this site if F^- couples with Eu^{3+}. Because there are six equivalent interstitial sites around the Eu^{3+} ion, the image intensity of the coupled F^- should be one-sixth of the intensities of the other F atomic images. Thus, we increased the maximum scale around the cross by a factor of 4 and found a distinct image, as shown inside the box in Fig. 5A. The distance between this image and the origin is 2.3 Å, which is close to the Eu–F bond length determined by XAFS. Although Eu^{3+}-interstitial F^- coupling has been proposed on the basis of the results obtained by spectroscopic and theoretical methods (*18*), we have directly proved its occurrence for the first time.

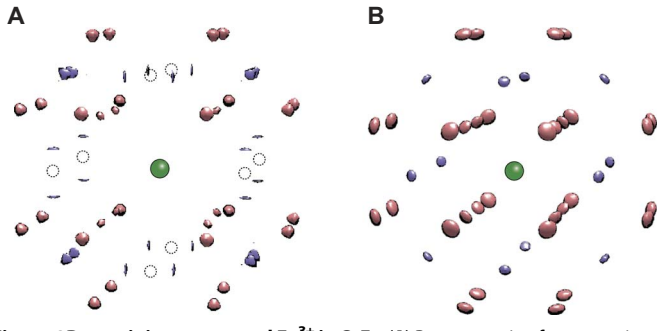

Fig. 4. 3D atomic images around Eu^{3+} in CaF_2. (**A**) Reconstruction from experimental hologram. (**B**) Reconstruction from calculated hologram. The calculation was carried out by assuming the simple substitution of Eu at Ca sites. No structural modification due to doping was assumed.

Figure 5B shows the F plane 1.35 Å above the Eu atom. Although the first- and second-neighbor images can be seen, more distant images cannot be observed, as indicated by the dashed circles. Moreover, other atomic images outside of the region with a radius of ~5.6 Å were also not visualized. The reason for this originates from the $\Delta|\mathbf{k}|$ range (wavelength range) of each single-wavelength hologram in our data processing. The $\Delta|\mathbf{k}|$ range is inversely proportional to the limit of the reconstructable range. On the other hand, the relatively weak first-neighbor F images indicate large positional fluctuations of F, because the fluctuation of an atom decreases the image intensity. Such a phenomenon has often been observed in local structures around dopants (*24*, *25*).

Cross sections of the split images are shown in Fig. 5C. The distance between the images is as large as 1.2 Å, revealing that the neighbor Ca atoms are displaced by 0.6 Å from the (001) plane. This phenomenon

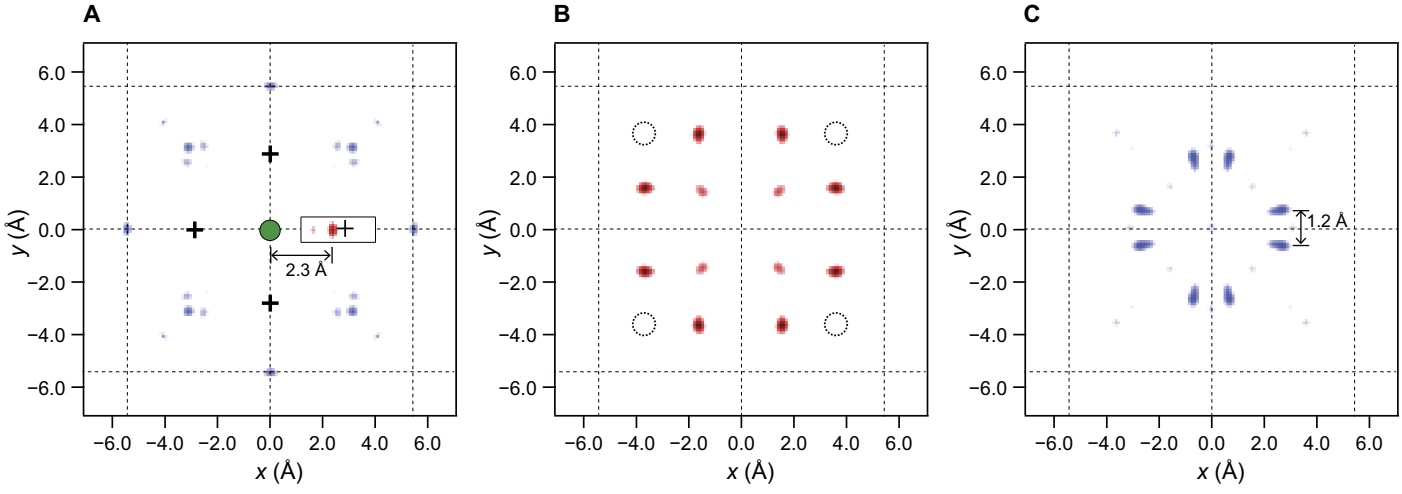

Fig. 5. 2D images at typical atomic planes. (**A**) Ca plane at z = 0.0 Å. The Eu atom was located at the origin. (**B**) F plane at z = 1.35 Å. (**C**) Ca plane at z = 2.70 Å.

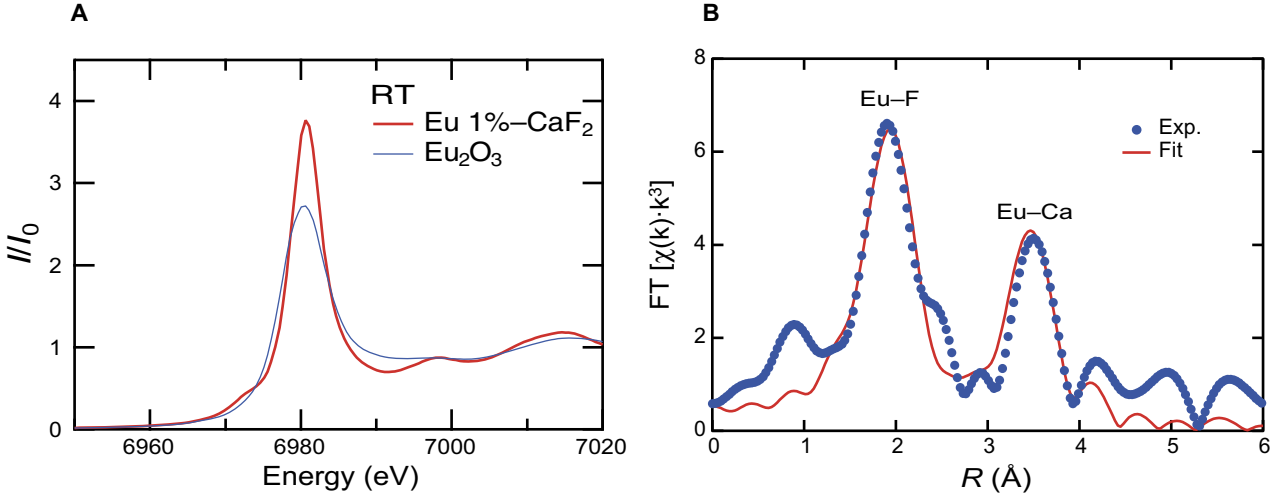

Fig. 6. XAFS result of Eu-doped CaF_2. (**A**) XANES spectra of the Eu-doped CaF_2 (red line) and a trivalent reference sample. (**B**) Magnitude of Fourier transform of EXAFS oscillation of Eu-doped CaF_2. Dotted and solid lines indicate experimental and calculated data, respectively.

might have been caused by the excessive charge of the Eu dopant, which was confirmed to be trivalent by the XAFS method (Fig. 6A). Because the Ca in CaF_2 is divalent, the excessive charge must have been compensated by a modification of the local structure. Moreover, this feature is supported by the EXAFS result in Fig. 6B for the Eu–Ca distance (4.00 Å), which is 0.13 Å longer than the Ca–Ca distance in pure CaF_2. Recently, we observed the large distortion of an As sublattice in a sphalerite $ZnSnAs_2$ thin film (*26*), and we found that the cation and anion sublattices are considerably different. Here, the local Ca sublattice distortion was larger than that of the local F sublattice closer to Eu. Note that Ca^{2+} should be strongly affected by Eu^{3+} beyond the surrounding F^- cage.

In summary, we have demonstrated multiple-wavelength neutron holography with the time-of-flight technique using a single crystal of Eu^{3+}-doped CaF_2. The present technique for the single-scan recording of a multiple-wavelength hologram is more efficient than the x-ray fluorescence holography technique for overcoming the problem of the low neutron intensity. The accurate atomic image obtained by using a number of different-wavelength holograms directly proved the existence of additional F^- ions at interstitial positions in Eu^{3+}-doped CaF_2. The efficiency of the measurement and the accuracy of the atomic images obtained by this method will provide a new means of studying local structure science.

MATERIALS AND METHODS

Sample preparation

In this experiment, we used a large single crystal of Eu-doped CaF_2, which was prepared at the Institute for Materials Research, Tohoku University. It was grown by the Czochralski method with a CaF_2 single-crystal seed. Pieces of a 4N-purity CaF_2 ingot (200 g) and 4N-purity EuF_3 powder (5.406 g) were charged in a pyrolytic graphite crucible, with a diameter and a length of 50 mm. The mixture of raw materials was premelted under an Ar and 5% CF_4 atmosphere to eliminate water, causing various defects such as subgrain boundaries, bubbles, and oxygen-related precipitates in the crystal. After the premelting, the sample was grown under an Ar flow. The seed and crucible were rotated in opposite directions at 15 and 1 rpm, respectively, and the pulling-up speed was set to 5 mm/hour. In this way, a crack-free Eu-doped CaF_2 single crystal with a diameter of 25 mm and a length of 45 mm was obtained. Using inductively coupled plasma optical emission spectrometry and x-ray fluorescence analysis, the concentration of Eu was estimated to be 1 at %. The x-ray diffraction pattern did not show a second phase upon Eu doping. The crystal system of CaF_2 is cubic with *cF*12 symmetry, and the lattice constant is a = 5.46 Å. For the neutron holography experiment, we finally cut the single crystal to a cylinder of dimensions 20 mm ϕ × 10 mm *t*.

Experimental setup for neutron holography

As shown in Fig. 2A, we constructed the setup of the neutron holography experiments in the experimental hutch of BL10 at MLF (Materials and Life Science Experimental Facility) of J-PARC, Tokai, Japan. The sample was mounted on a two-axis (ϕ and θ) rotation stage; ϕ and θ are the azimuthal and polar angles, respectively. One of the <001> axes of the Eu-doped CaF_2 was set to be parallel to the direction of the incoming neutron beam, and one of the {100} planes was set to be horizontal when ϕ and θ were equal to 0°. The neutron beam size was 25 × 25 mm^2. Prompt γ rays were detected by a BGO ($Bi_4Ge_3O_{12}$) scintillation counter, which was connected to a GateNet module (the event-recording data acquisition system of J-PARC) to record the time-of-flight spectrum of the γ ray intensity at each ϕ and θ (see Fig. 1B). The scan ranges were $0° \le \phi \le 360°$ and $20° \le \theta \le 150°$. The scintillation counter was fixed adjacent to the stage, and it was covered with lead blocks except at the front to avoid the detection of unwanted γ rays. The distance between the counter and the sample was 150 mm. The measurement time for each scan was 10 hours. We carried out a total of nine scans and then summed the data sets to increase the statistical quality.

Absorption correction

The amplitude of a hologram is affected by the absorption of neutrons and γ rays by a sample. Here, we discuss the absorption effect using the sample shape model in Fig. 2B, which is similar to the shape of our sample. Most of the sample was inside the neutron beam because its size was 25 × 25 mm^2. Some neutrons traveled along the path of length ℓ_z to the γ ray–emitting point $\mathbf{r}$, and the γ rays traveled along the path of length ℓ_x. The γ ray detector was set perpendicular to the neutron beam, where ℓ_x and ℓ_z are functions of $\mathbf{r}$, ϕ, and θ. Although γ rays were detected with an acceptance angle of 28°, we used the approximated model in Fig. 2B for the calculation. The incident neutron intensity at the emitting point $\mathbf{r}$, $I(\ell_z)$, can be written by

$$I(\ell_z) = I_0 \exp(-\mu_N \rho \ell_z (1 + \chi(\mathbf{k}))) \quad (1)$$

where I_0 is the incident neutron beam before the sample, μ_N is the neutron absorption coefficient, and ρ is the density of the CaF_2 crystal. In principle, $\chi(\mathbf{k})$ is the same as holographic oscillation, and it gives the angular dependence of the absorption. Using Eq. 1, the γ ray intensity at $\mathbf{r}$, $P(\ell_z)$, is calculated as

$$P(\ell_z) = I_0 C (1 + \chi(\mathbf{k})) \exp(-\mu_N \rho \ell_z (1 + \chi(\mathbf{k}))) \quad (2)$$

where C is a constant. By integrating $p(\ell_z)$ from 0 to the depth D, we can obtain the total γ ray yield from this path

$$\int_0^D P(\ell_z) d\ell_z = \frac{I_0 C}{\mu_N \rho} \{1 - \exp(-\mu_N \rho D (1 + \chi(\mathbf{k}))\} \quad (3)$$

From this equation, the holographic signal cannot be measured if depth D is sufficiently large to absorb most of the neutrons.

Next, because the γ rays are absorbed along the path of length ℓ_x, the detected γ ray intensity, $P(\ell_x,\ell_z)$, is calculated using Eq. 2 as

$$P(\ell_x,\ell_z) = I_0 C' (1 + \chi(\mathbf{k})) \exp(-\mu_N \rho \ell_z (1 + \chi(\mathbf{k}))) \cdot \exp(-\mu_\gamma \rho \ell_x) \quad (4)$$

where C' is a constant, and μ_γ is the absorption coefficient of the γ rays. By integrating $P(\ell_x,\ell_z)$ over the irradiated volume of the sample, we can obtain the detected γ ray yield as

$$Y_h(\phi, \theta) = \iiint P(\ell_x(\mathbf{r}, \phi, \theta),\ \ell_z(\mathbf{r}, \phi, \theta)) dV \quad (5)$$

In the experiment, we normalized Y_h by the background intensity Y_B. By applying Eq. 5 to our experimental conditions, we can obtain the decrement in the amplitude of holographic oscillation $\chi(\mathbf{k})$ at each θ, as shown in Fig. 2C. Using this decrement, we corrected the amplitude of the observed hologram.

XAFS measurement

The XAFS experiments at the Eu LIII absorption edge (6.9769 keV) were performed at BL-12C of the Photon Factory of High Energy Accelerator Research Organization (KEK), Tsukuba, Japan. The spectra were obtained in the transmission mode. The intensities of the incident and transmitted x-ray beams (I_0 and I) were monitored using two ionization chambers, whose lengths were 140 and 270 mm, respectively. As detector gases in the chambers, we used pure N_2 for the incident beam and N_2 (50%)–Ar (50%) for the transmitted beam. The sample of Eu-doped CaF_2 was prepared from the single crystal used for the neutron holography experiments. Spectra of Eu_2O_3 were also measured the same as those of a trivalent standard sample.

Data processing

The times of flight were converted to the wavelengths of incoming neutrons exciting Eu nuclei. Then, the profiles were divided into 34 $|\mathbf{k}|$ regions between 4.04 and 8.19 $Å^{-1}$, where $\mathbf{k}$ is the wave number vector in the reciprocal lattice space in the hologram, which can be expressed by the following equations

$$k_x = \frac{2\pi}{\lambda}\cos\phi\sin\theta \quad (6)$$

$$k_y = \frac{2\pi}{\lambda}\sin\phi\sin\theta \quad (7)$$

$$k_z = \frac{2\pi}{\lambda}\cos\theta \quad (8)$$

λ is the wavelength of the incoming neutrons exciting a Eu nucleus.

Here, the lack of a suitable incident monitor for the neutron beam was a serious problem. Because the intensity of the pulsed neutrons fluctuated markedly, normalization with an incident monitor was necessary to extract the weak holographic oscillation, whose intensity was approximately 0.1% of the total γ ray intensity. Here, we used integrated intensities below $|\mathbf{k}| = 1.12$ $Å^{-1}$ ($\lambda = 5.6$ Å) as the incident monitor (yellow region in the inset of Fig. 1B), and we normalized the γ ray intensity in each $|\mathbf{k}|$ region by the integrated intensity. Because $|\mathbf{k}| = 1.12$ $Å^{-1}$ is the diffraction limit of CaF_2, obstructive neutron standing-wave lines did not appear in the 2D intensity pattern below $|\mathbf{k}| = 1.12$ $Å^{-1}$. Moreover, because holographic oscillations were also smeared out by summing the intensity patterns in a wide $|\mathbf{k}|$ range, the integrated intensity below $|\mathbf{k}| = 1.12$ $Å^{-1}$ became a good intensity monitor.

To confirm the validity of our normalization process, we calculated holograms of the Eu-doped CaF_2 with a step of $\Delta|\mathbf{k}| = 0.127$ $Å^{-1}$ and obtained the 2D incident monitor pattern in a manner similar to that previously described above. In the calculated model, Eu is replaced by Ca in the CaF_2 crystal. As shown in Fig. 4B, a 3D real-space image was reconstructed from the theoretical holograms normalized by the 2D incident monitor pattern. This image is similar to the images obtained from the theoretical holograms without the normalization. Thus, the present normalization process was judged to be valid.

REFERENCES AND NOTES

1. A. Szöke, in *Short Wavelength Coherent Radiation: Generation and Applications*, D. T. Attwood, J. Boker, Eds. (AIP Conference Proceedings No. 147, American Institute of Physics, 1986), pp. 361–367.
2. G. R. Harp, D. K. Saldin, B. P. Tonner, Scanned-angle x-ray photoemission holography with atomic resolution. *Phys. Rev. B* **42**, 9199–9202 (1990).
3. M. Tegze, G. Faigel, X-ray holography with atomic resolution. *Nature* **380**, 49–51 (1996).
4. D. P. Woodruff, Adsorbate structure determination using photoelectron diffraction: Methods and applications. *Surf. Sci. Rep.* **62**, 1–38 (2007).
5. K. Hayashi, M. Matsui, Y. Awakura, T. Kaneyoshi, H. Tanida, M. Ishii, Local-structure analysis around dopant atoms using multiple energy x-ray holography. *Phys. Rev. B* **63**, 041201 (2001).
6. W. Hu, K. Hayashi, T. Fukumura, K. Akagi, M. Tsukada, N. Happo, S. Hosokawa, K. Ohwada, M. Takahasi, M. Suzuki, M. Kawasaki, Spontaneous formation of suboxidic coordination around Co in ferromagnetic rutile $Ti_{0.95}Co_{0.05}O_2$ film. *Appl. Phys. Lett.* **106**, 222403 (2015).
7. W. Hu, K. Hayashi, K. Ohwada, J. Chen, N. Happo, S. Hosokawa, M. Takahasi, A. A. Bokov, Z.-G. Ye, Acute and obtuse rhombohedrons in the local structures of relaxor ferroelectric $Pb(Mg_{1/3}Nb_{2/3})O_3$. *Phys. Rev. B* **89**, 140103 (2014).
8. T. Gog, P. M. Len, G. Materlik, D. Bahr, C. S. Fadley, C. Sanchez-Hanke, Multiple-energy x-ray holography: Atomic images of hematite (Fe_2O_3). *Phys. Rev. Lett.* **76**, 3132–3135 (1996).
9. B. Sur, R. B. Rogge, R. P. Hammond, V. N. P. Anghel, J. Katsaras, Atomic structure holography using thermal neutrons. *Nature* **414**, 525–527 (2001).
10. L. Cser, G. Török, G. Krexner, I. Sharkov, B. Faragó, Holographic imaging of atoms using thermal neutrons. *Phys. Rev. Lett.* **89**, 175504 (2002).
11. L. Cser, G. Török, G. Krexner, M. Prem, I. Sharkov, Neutron holographic study of palladium hydride. *Appl. Phys. Lett.* **85**, 1149–1151 (2004).
12. L. Cser, G. Krexner, M. Markó, I. Sharkov, G. Török, Direct observation of local distortion of a crystal lattice with picometer accuracy using atomic resolution neutron holography. *Phys. Rev. Lett.* **97**, 255501 (2006).
13. K. Hayashi, K. Ohoyama, S.-i. Orimo, H. Takahashi, K. Shibata, Neutron holography and diffuse scattering of palladium hydride. *Phys. Rev. B* **91**, 024102 (2015).
14. A. Szakái, M. Markó, L. Cser, Local distortions revealed by neutron holography in $SnCd_{0.0026}$ alloy. *Phys. Rev. B* **93**, 174115 (2016).
15. R. M. Brugger, in *Thermal Neutron Scattering*, P. A. Egelstaff, Ed. (Academic Press, 1965), pp. 54–96.
16. K. Oikawa, F. Maekawa, M. Harada, T. Kai, S. Meigo, Y. Kasugai, M. Ooi, K. Sakai, M. Teshigawara, S. Hasegawa, M. Futakawa, Y. Ikeda, N. Watanabe, Design and application of NOBORU—NeutrOn Beam line for Observation and Research Use at J-PARC. *Nucl. Instrum. Methods Phys. Res. A* **589**, 310–317 (2008).
17. F. Maekawa, M. Harada, K. Oikawa, M. Teshigawara, T. Kai, S.-i. Meigo, M. Ooi, S. Sakamoto, H. Takada, M. Futakawa, T. Kato, Y. Ikeda, N. Watanabe, T. Kamiyama, S. Torii, R. Kajimoto, M. Nakamura, First neutron production utilizing J-PARC pulsed spallation neutron source JSNS and neutronic performance demonstrated. *Nucl. Instrum. Methods Phys. Res. A* **620**, 159–165 (2010).
18. C. Plettner, G. Pausch, F. Scherwinski, C. M. Herbach, R. Lentering, Y. Kong, K. Römer, M. Grodzicka, T. Szcześniak, J. Iwanowska, M. Moszyński, CaF_2(Eu): An "old" scintillator revisited. *J. Instrum.* **8**, P06010 (2013).
19. A. Rauch, W. Waschkowski, in *Neutron Data Booklet*, A.-J. Dianoux, G. Lander, Eds. (Institut Laue-Langevin, 2002), pp. 1.1-8–1.1-19.
20. P. Korecki, D. V. Novikov, M. Tolkiehn, G. Materlik, Extinction effects in x-ray holographic imaging with internal reference. *Phys. Rev. B* **69**, 184103 (2004).
21. J. J. Barton, Removing multiple scattering and twin images from holographic images. *Phys. Rev. Lett.* **67**, 3106–3109 (1991).
22. J. Corlish, C. R. A. Catlow, P. W. M. Jacobs, S. H. Ong, Defect aggregation in anion-excess fluorites. Dopant monomers and dimers. *Phys. Rev. B* **25**, 6425–6438 (1982).
23. D. Chen, L. Lei, J. Xu, A. Yang, Y. Wang, Abnormal size-dependent upconversion emissions and multi-color tuning in Er^{3+}-doped CaF_2–YbF_3 disordered solid-solution nanocrystals. *Nanotechnology* **24**, 085708 (2013).
24. S. Hosokawa, N. Happo, T. Ozaki, H. Ikemoto, T. Shishido, K. Hayashi, Extent and features of lattice distortion around Ga impurity atoms in InSb single crystal. *Phys. Rev. B* **87**, 094104 (2013).
25. N. Happo, M. Fujiwara, K. Tanaka, S. Hosokawa, K. Hayashi, Lattice distortions in γ-ray detector material $Cd_{0.96}Zn_{0.04}Te$ probed by Zn Kα x-ray fluorescence holography. *J. Electron Spectrosc. Relat. Phenom.* **181**, 154–158 (2010).
26. K. Hayashi, N. Uchitomi, K. Yamagami, A. Suzuki, H. Yoshizawa, J. T. Asubar, N. Happo, S. Hosokawa, Large as sublattice distortion in sphalerite $ZnSnAs_2$ thin films revealed by x-ray fluorescence holography. *J. Appl. Phys.* **119**, 125703 (2016).

Acknowledgments: The neutron experiments were performed at beamline BL10, with the approval of J-PARC (proposal no. 2012B0248). The XAFS experiment was performed under a user program of Photon Factory–KEK (proposal no. 2015P007). **Funding:** This work was partially supported by a Japan Society for the Promotion of Science Grant-in-Aid for Scientific

Research (B) (no. 16H03849) and the Scientific Research on Innovative Areas "3D Active-Site Science" (nos. 26105006 and 26105013). **Author contributions:** K.H., K.O., N.H., and S.H. performed the neutron hologram measurements with help from M.H. T.S. and K.Y. performed the crystal growth. K.O. and H.N. performed the XAFS measurements. K.H., K.O., T.M., and Y.I. performed the data processing. K.H. wrote the paper. **Competing interests:** The authors declare that they have no competing interests. **Data and materials availability:** All data needed to evaluate the conclusions in the paper are present in the paper. Additional data related to this paper may be requested from the authors at khayashi@nitech.ac.jp.

Submitted 27 January 2017
Accepted 13 July 2017
Published 18 August 2017
10.1126/sciadv.1700294

Citation: K. Hayashi, K. Ohoyama, N. Happo, T. Matsushita, S. Hosokawa, M. Harada, Y. Inamura, H. Nitani, T. Shishido, K. Yubuta, Multiple-wavelength neutron holography with pulsed neutrons. *Sci. Adv.* **3**, e1700294 (2017).

Multiple-wavelength neutron holography with pulsed neutrons

Kouichi Hayashi, Kenji Ohoyama, Naohisa Happo, Tomohiro Matsushita, Shinya Hosokawa, Masahide Harada, Yasuhiro Inamura, Hiroaki Nitani, Toetsu Shishido and Kunio Yubuta

Sci Adv **3** (8), e1700294.
DOI: 10.1126/sciadv.1700294